Geometrical Modelling of 3D Woven Reinforcements for Polymer Composites: Prediction of Fabric Permeability and Composite Mechanical Properties

Xuesen Zeng, Louise P. Brown, Andreas Endruweit*, Mikhail Matveev, Andrew C. Long

Faculty of Engineering – Division of Materials, Mechanics & Structures,
University of Nottingham, University Park, Nottingham, NG7 2RD, U.K.
*corresponding author. andreas.endruweit@nottingham.ac.uk, fax 0044 (0)115 9513800

Abstract

For a 3D orthogonal carbon fibre weave, geometrical parameters characterising the unit cell were quantified using micro-Computed Tomography and image analysis. Novel procedures for generation of unit cell models, reflecting systematic local variations in yarn paths and yarn cross-sections, and discretisation into voxels for numerical analysis were implemented in TexGen. Resin flow during reinforcement impregnation was simulated using Computational Fluid Dynamics to predict the in-plane permeability. With increasing degree of local refinement of the geometrical models, agreement of the predicted permeabilities with experimental data improved significantly. A significant effect of the binder configuration at the fabric surfaces on the permeability was observed. In-plane tensile properties of composites predicted using mechanical finite element analysis showed good quantitative agreement with experimental results. Accurate modelling of the fabric surface layers predicted a reduction of the composite strength, particularly in the direction of yarns with crimp caused by compression at binder cross-over points.

Keywords: A. 3-Dimensional reinforcement, B. Mechanical properties, C. Numerical analysis, E. Resin flow

1. Introduction

In thick composite components, multiple thin layers of fabrics with two-dimensional (2D) architectures can be replaced by thick three-dimensional (3D) fibrous structures as reinforcements. As discussed by Mouritz et al. [1], 3D textile processes, in particular highly versatile weaving processes, allow the near net-shape manufacture of reinforcements with complex geometries. 3D woven reinforcements consist typically of layers of aligned non-crimp yarns with alternating orientation along the fabric weft and warp directions, and additional binder yarns, which follow paths through the fabric thickness and hold the non-crimp layers together.

In composites, the non-crimp yarns in each fabric layer show generally better axial mechanical properties than the crimped yarns in most 2D reinforcements. The presence of binder yarns provides toughness and resistance to delamination but tends to reduce mechanical in-plane properties compared to purely uni-directionally aligned layers. However, mechanical in-plane properties of composites were found to be higher for 3D woven reinforcements than for multi-layer plain weave reinforcement [2, 3]. For the case of frequently used 3D orthogonal woven reinforcements, the mechanical properties of composites have been addressed in detail in a variety of studies. The in-plane stiffness and strength have been investigated experimentally, analytically and numerically, e.g. by Tan et al. [4, 5]. Carvelli et al. [6] characterised the fatigue behaviour in tension. The response to static and impact transverse loading was studied, e.g. by Luo et al. [7]. Mohamed and Wetzel [8] described in detail the influence of the variation of fabric parameters on the properties of a component.

Regarding reinforcement processing properties, forming of an orthogonal weave was characterised by Carvelli et al. [9] in terms of in-plane biaxial tension and shear behaviour. Due to increased thickness and the through-thickness fixation of the yarns, the drapability of

3D woven reinforcements, i.e. the formability to doubly-curved surfaces, tends to be reduced compared to 2D fabrics. However, this is less relevant, since the reinforcements can be manufactured to near net-shape [1]. On the other hand, the reinforcement compressibility is highly relevant, since it determines the fibre volume fraction in the reinforcement. This affects the reinforcement impregnation with a liquid resin system in Liquid Composite Moulding (LCM) processes, which are particularly suited for the manufacture of thick components with 3D woven reinforcements, and the mechanical properties of the finished component. Some data for a 3D fabric, suggesting significantly higher stiffness in compression than for a random mat, were given by Parnas et al. [10]. Potluri and Sagar [11] studied the compaction behaviour of several fabrics with interlacing weaving patterns in more detail and applied an energy minimisation technique to compaction modelling, which generally showed good agreement with experimental results. Endruweit and Long [12] observed experimentally that local reduction of the gap height between the fibre bundles is significant in compression of an angle-interlock weave with offset of layers. On the other hand, the main compression mechanism for an orthogonal weave was found to be compaction of the fibre bundles. This results in higher compressibility for the angle-interlock weave than for the orthogonal weave.

The flow of liquid resin during fabric impregnation in LCM processes is more complex than in thin fibrous structures because of the presence of additional through-thickness yarns. Information on impregnation behaviour, characterised by the reinforcement permeability, is sparse for 3D reinforcements. Experimental data published by Parnas et al. [10] suggest that the in-plane and through-thickness permeabilities of 3D woven fabrics are in the same order of magnitude as those of 2D fabrics at similar fibre volume fractions. Elsewhere, it was suggested that 3D orthogonal woven fabrics have significantly higher in-plane permeability than 2D fabrics (woven and knitted) at identical fibre volume fraction [13]. Numerical predictions of the permeability of an orthogonal weave by Ngo and Tamma [14] indicated that the in-plane permeability is high compared to the through-thickness permeability, and qualitative agreement with experimental observations was found. Song et al. [15] predicted the permeability tensor for a 3D braided textile (similar to an interlacing weave). While they also found higher values for the in-plane than for the through-thickness permeability, experimental results were overestimated by significant margins. Endruweit and Long [12] modelled the influence of inter-yarn gap widths and the pattern and dimensions of binder yarns on the in-plane permeabilities of 3D woven fabrics. Experimental data suggested that in-plane permeabilities reflect the reduction of inter-yarn gap spaces during fabric compaction. Through-thickness permeabilities were found to be enhanced by through-thickness channels formed around the binder yarns.

A major challenge in predicting the processing and performance characteristics of composite materials is the complex hierarchical structure and its local variation, in particular if 3D woven reinforcements are used. This is reflected in growing research efforts for meso-scale geometry characterisation [16-19] and modelling [20-23]. This study aims at experimental quantification of representative geometrical parameters for a 3D woven fabric and generation of unit cell models at a high level of geometrical detail, including systematic local variations in yarn paths and yarn cross-sections. Based on these models, numerical methods are implemented to predict the reinforcement permeability and the mechanical performance of the finished composite.

2. Geometrical characterisation

As an example, a carbon fibre orthogonal weave with the specifications listed in Table 1 was characterised in this study. The internal geometry of the fabric was characterised at different compaction levels by X-ray micro-Computed Tomography (μ-CT) analysis. A Phoenix Nanotom (GE Sensing & Inspection Technologies GmbH) was used for μ-CT scanning of small samples, which were slightly larger than unit cell size of the 3D woven reinforcement. While the dry fabric was scanned at no compaction, composite specimens were produced to allow the deformed geometry in the compressed fabric to be captured. To obtain good image contrast for carbon fibre composites, which show low X-ray energy absorption, the power was set to a voltage of 40 keV and a current of 240 μA, and a Molybdenum target (emitting radiation at a relatively small wavelength, which is absorbed by low-density materials) was used. The image resolution is between 7 μm and 20 μm, depending on the geometrical dimensions of the scan sample.

While the 3D image data can be analysed by taking measurements manually slice by slice, contrast-based image processing (as illustrated in Fig. 1) and quantitative evaluation was automated using the MatLab® Image Toolbox. To determine shapes and dimensions of yarns and inter-yarn gaps in Fig. 1E, the images are segmented into square cells, allowing focusing on individual gaps as in Fig. 1A. Filtering techniques are applied to reduce noise and suppress small-scale features (Fig. 1B). The resulting greyscale image is then converted into a binary image (Fig. 1C), implying that information on defects such as trapped air or cracks caused by thermal shrinkage may be lost. The final stage is to remove features unrelated to gaps by assessing the size, roundness, aspect ratio and position of segmented objects (Fig. 1D). The result is a black and white image showing the inter-yarn gaps in cross-section (Fig. 1F). For each identified gap, continuity throughout the entire range of slices can be tracked.

Quantitative evaluation of the images includes measurement of area, A_c, and height, h, of gaps in a cross-section, and yarn spacing, l, i.e. the distance between the centroids of two neighbouring gaps. At given filament radius, r, and number of filaments, N, in each yarn, the fibre volume fraction in each yarn cross-section can be calculated according to

$$V_f = \frac{N \pi r^2}{h l - A_c} \quad . \tag{1}$$

To measure gaps in weft and warp directions, the 3D images are re-sliced and analysed in each direction. Data for composites at two different fibre volume fractions, i.e. thicknesses, *H*, are listed in Table 2.

3. Geometrical modelling

3.1 General considerations

Reliable numerical analysis of reinforcement processing properties and composite mechanical performance requires accurate description of the reinforcement geometry. Since detailed modelling of full-size fabric specimens is not realistic, the fabric architecture is represented by a unit cell, by definition the smallest repetitive (by translation) unit in a fabric. Since yarns in a fabric are not perfectly fixated but have some mobility, all textiles tend to exhibit some degree of stochastic variability. Thus, unit cell modelling always implies idealised approximation of the exact geometry. Here, image analysis indicates that the degree of geometric variability in the 3D woven reinforcement is relatively low (Table 2), at similar level as observed by Desplentere et al. [24]. Thus, unit cell modelling can be expected to give a relatively accurate approximation of the actual (local) architecture.

To take experimentally observed variabilities into account, Desplentere et al. [24] used series of unit cell models with standardised geometry and varying dimensions as input for Monte-Carlo simulations of mechanical properties. This study aims to identify the dominant geometrical features in the 3D woven reinforcement and deduce a generic set of rules to generate input parameters for the unit cell model. The fundamental steps of textile geometry modelling and mesh generation for numerical analysis using the software TexGen [25, 26] will be discussed in the following.

3.2 Yarn paths and crimp

Yarn paths are modelled in TexGen by interpolating a number of appropriately positioned master nodes using cubic Bézier splines to ensure the periodic continuity of yarn paths in a unit cell. In an orthogonal weave, paths for non-crimp warp and weft yarns can be treated as straight parallel lines at constant spacing. Exceptions are the surface layers of weft yarns, where crimp is introduced as the fabric compaction level increases (Fig. 2). The magnitude of crimp in the weft yarns at crossover points with the binder corresponds to the local thickness of the compressed binder yarn, modelled in TexGen by offsetting the through-thickness coordinate of the corresponding master node on the weft yarn.

The path of the binder yarn varies considerably with increasing compaction level as illustrated in Fig. 2. For uncompressed fabric, the binder has slight S-shaped curvature (Fig. 2A). At low compaction levels, the total fabric thickness is reduced, resulting in increased curvature of the binder (Fig. 2B). At high compaction levels, warp and weft yarns are flattened and widened, reducing inter-yarn gap spaces. This imposes geometrical constraints for the binder yarn, which is straightened in the fabric, and, since the total length does not change, forms loops in the surface layers of weft yarns (Fig. 2C).

To take into account the different constraints for the binder yarn path in TexGen, a number of reference nodes are placed on the periphery of weft yarns in different layers. As illustrated in Fig. 3, 9 nodes are placed at a distance of half the thickness of the binder yarn from the perimeter of the weft yarns. The distance of nodes on the binder yarn path to the weft yarns cannot be smaller than the distance of these reference nodes. For uncompressed fabric (Fig. 2A), only nodes on the surface weft yarns are needed to define the binder yarn path. For highly compressed fabric as in Fig. 2C, the shape of the binder yarn includes the corner nodes of weft yarns on each internal layer.

3.3 Yarn cross-section

The cross-sectional shape of a multifilament yarn is determined by interaction with neighbouring yarns. Of particular significance is the influence of the binder yarn on the surface layers of weft yarns, which results in different dimensions and shape of yarns on the fabric surfaces and the internal layers (Table 2). This is also reflected in the differences in V_f for the surface layers and internal layers observed by Karahan et al. [17]. In TexGen, yarn cross-sections are approximated by power-ellipses, special cases of a superellipse [27], which are described by points (x, y) with

$$x(\nu) = \frac{w}{2}\cos(2\pi\nu) \qquad 0 \le \nu \le 1 \tag{2}$$

and

$$y(\nu) = \begin{cases} \frac{h}{2}\sin^n(2\pi\nu) & \text{if} \quad 0 \le \nu < 0.5 \\ -\frac{h}{2}(-\sin(2\pi\nu))^n & \text{if} \quad 0.5 \le \nu \le 1 \end{cases} . \tag{3}$$

Here, the exponent, n, describes the shape of the power-ellipse, w is the yarn width, h is the yarn height, and the parameter ν indicates the angular coordinate at the ellipse centre relative to the major axis.

The characteristics of power-ellipses are shown in Figure 4A for different values of n, resulting in circular, elliptical, rounded rectangular and lenticular shapes. In real fabrics, yarn cross-sections are often asymmetric. To address this issue, hybrid cross-sections can be generated in TexGen, allowing different curve sections to be joined. An example is given in Fig. 4B, where a hybrid of two power-ellipses is fitted to an actual yarn cross-section. The upper ($0 \le \nu \le 0.5$) and lower ($0.5 \le \nu \le 1$) halves of the cross-section share the same width, w, but differ in height, h, and power, n. The parameters in Eqs. (2) and (3) are determined by measuring 6 points, P_1 to P_6. The intersection between lines P_1P_2 and P_3P_4 is the origin of its Cartesian coordinate-system, O. The distance P_1P_2 corresponds to the width, w. The distances OP_3 and OP_4 are half the heights of respective upper and lower power-elliptical sections. The points P_5 and P_6 are defined on the curves such that the tangents include angles of approximately 45° or 135° with the major axis. Using the measured (x, y) either at point P_5 or P_6, the respective exponents can be determined according to

$$n = \frac{2\log(2\,y/h)}{\log\left(1-(2\,x/w)^2\right)} \quad . \tag{4}$$

3.4 Unit cell

While the fabric architecture is defined by the parameters listed in Table 1, the input parameters for generating a unit cell model are specified in Table 2. The basic structure of the yarn paths can be generated automatically using the “3D wizard” in TexGen. A series of dialogs allow entry of number of warp and weft yarns, as well as the number of layers of each and the ratio of binder to warp yarns. The width, height, spacing and cross-sectional shape can be specified for each set of yarns. A weave pattern dialog allows specification of the weave pattern, and then the fabric is automatically generated with nodes on the yarn paths at each crossover point between warp or binder yarns and weft yarns. Extra nodes are positioned along the binder yarns to follow the contour of the outer weft yarns as described in Section 3.2.

The geometric definitions of the yarn paths and cross-sections described in Sections 3.2 and 3.3 were implemented manually as refinements for the models used to generate the results shown in the following sections. For simplification, it was assumed that all yarns other than weft yarns on the fabric surfaces, which were refined locally by introducing crimp and variable cross-sections at crossover points with binder yarns, have constant cross-section and constant spacing along the yarn axes.

Subsequent to the results obtained using these manual refinements, a ‘refine’ option has been developed in TexGen to implement the refinements automatically. An additional parameter, target fabric thickness, is specified after which the TexGen software adjusts the yarns, following the process shown in the flowchart in Fig. 5. Throughout the process, the volume fractions of the yarns are monitored so that they are maintained within realistic limits. Intersections in the model are also minimised by the process which constrains yarns to the areas available and shapes the binder yarns to follow the contour of the outer weft yarns. The fabrics generated using this automatic refinement with the data given in Tables 1 and 2 are shown in Fig. 6. Figure 6A shows the orthogonal weave with the refine option selected but no change to the initial fabric thickness of 6.32 mm. The refinement here is limited to the binder yarns and the outer weft yarns. Figures 6B and 6C show the fabric compacted to thicknesses of 5.03 mm and 4.43 mm. Figure 6C shows the addition of a small amount of crimp in the outer weft yarn, necessary to achieve this degree of compaction. This is also observed experimentally, e.g. in the μ-CT image in Fig. 7B. Comparison with the μ-CT images shows that TexGen is capable of automatically modelling the geometry realistically down to a fabric thickness of 5.03 mm (V_f = 0.55). At a higher compaction level (thickness 4.43 mm), deviations between the automatically generated TexGen model and the real geometry occur, noticeably in the surface yarn cross-sections. The refine option is available as part of the release version of the TexGen software but does still require validation for a larger range of 3D fabrics.

3.5 Discretisation

In unit cell models of textile fabrics, discretisation for numerical analysis is relatively straightforward for yarns. However, inter-yarn spaces, which represent the main flow domains in analysis of impregnating resin flow and resin-only zones in mechanical analysis of composite performance, tend to have complex geometries. Particular problems are caused by very small inter-yarn spaces, which can have a significant effect on the properties and thus are not negligible. These geometries are hard to discretise by conformal meshing. Thus, TexGen was used for automated voxel meshing of the unit cell domain, i.e. the domain was discretised into a regular hexahedral grid, where properties of either yarns or gaps were assigned to voxels depending on the centre point locations. While previous studies for prediction of fabric permeability based on Computational Fluid Dynamics (CFD) [28-30] and analysis of composite mechanical properties [31, 32] proved the robustness of voxel meshing, it was also shown that uniform meshing may result in computational inefficiency and that the solution may be mesh-dependent. In this study, minimum mesh densities for analysis of permeabilities and mechanical properties were chosen based on convergence tests.

4. Fabric permeability analysis

4.1 Flow modelling

To analyse resin flow during reinforcement impregnation in composites processing, steady-state laminar flow of an incompressible Newtonian fluid was simulated on the domain of the unit cell of the 3D weave. Flow through inter-yarn gaps was modelled as Navier-Stokes flow, while flow in yarns, modelled as porous media, was assumed to be governed by Darcy's law. For the latter case, axial and transverse yarn permeabilities as input parameters were calculated using Gebart's analytical model for hexagonal fibre packing [33]. The filament diameter was assumed to be 7 μm.

At all permeable interfaces, conservation of fluid mass and momentum was ensured. At the interfaces between porous yarns and inter-yarn flow channels, where the problem of coupling Navier-Stokes flow and Darcy flow occurs, fluid pressure and the normal component of the flow velocity were assumed to be continuous. The component of the fluid velocity tangential to the yarn surface was also assumed to be continuous (no-slip boundary), which is justified since inter-yarn gap spaces are approximately one order of magnitude larger than pore spaces in the yarns [34]. Use of a slip boundary condition (Beavers-Joseph boundary condition [35]) would be essential if the dimensions of inter-yarn gaps were comparable to the dimensions of intra-yarn pores. In this case, slip at the yarn surface would contribute to the permeability of the fabric, which would be implied to be extremely tightly woven. However, this effect is negligible for typical textile reinforcements. Translational periodic constraints, applied together with a flow-driving pressure drop, were set on opposite boundary faces of the textile unit cell domain in weft and warp direction to represent a continuous reinforcement. No-slip wall boundary conditions were specified at the impermeable top and bottom faces of the domain to simulate flow along the mould surfaces during in-plane fabric impregnation. The fluid was assumed to be incompressible with constant viscosity.

The equations describing the flow problem were solved using the CFD code ANSYS® CFX 12.0 on a hexahedral voxel mesh, where properties of either the flow channel domain or yarn volume were attributed to the voxels. The saturated in-plane permeability in warp and weft direction as well as the saturated through-thickness permeability was calculated based on Darcy's law from the average pressure drop across the unit cell and the flow rate obtained from the CFD simulation of flow in the respective directions, implying a process of volumetric homogenisation. The sensitivity of the CFD calculations to the mesh density was assessed based on convergence of the predicted in-plane permeability for the 3D weave at 25 × 25 × 25 voxels (warp × weft × thickness), 50 × 50 × 50 voxels, 100 × 100 × 100 voxels, and 200 × 200 × 200 voxels. To obtain a reasonable balance between computation time and accuracy, the number of voxels was chosen as 50 × 50 × 50 for the unit cell mesh. It was also observed that flow velocities are typically three orders of magnitude smaller in the yarns than in the inter-yarn gaps, suggesting that flow in the gaps dominates the permeability for this material.

4.2 Results and discussion

To assess the sensitivity of permeability prediction to the level of detail in geometrical textile modelling, unit cell models for a given fibre volume fraction (H = 5.0 mm, V_f = 0.55) were refined incrementally as described in Section 3. The geometrical variations considered in modelling are illustrated in Fig. 7. As a starting point, a unit cell of the orthogonal weave was generated with straight yarns and constant elliptical cross-sections (average dimensions based on data in Table 2). Successively, varying binder cross-sections (Fig. 7A), deformation of weft yarns on the fabric surface (“dimples”, Fig. 7B), and different yarn cross-sections in warp and weft direction (Fig. 7C) were introduced. The permeabilities derived from CFD simulations at different level of refinement are plotted together with experimental data [12] in Fig. 8, which illustrates how local geometrical refinement tends to improve the accuracy of permeability prediction. The effect is particularly strong for the permeability in the warp direction. This is overestimated by a significant amount if deformation of weft yarns on the fabric surfaces and changes in bundle shape are not considered, and artificial gaps between the fabric surfaces and the tool surfaces are generated in the model. Also in warp direction, the subtle refinement in yarn cross-section (Fig. 7C) allows more accurate representation of flow channel interruption due to tight contact between warp and binder yarns, leading to a significant drop in prediction which approaches the measured permeability (Fig. 8). The selected voxel mesh density proved sufficient to capture this important geometry refinement. The same principles for geometrical unit cell modelling were applied to the reinforcement at a higher fibre volume fraction, $V_f = 0.67$, although details of the complex deformation of the highly compacted binder yarn (as in Fig. 6C) are difficult to reproduce accurately.

Figure 9 shows a comparison of in-plane permeability data derived from CFD simulations with experimental data at different V_f. While the experimental data [12] show large scatter, particularly at low V_f, they suggest that there is a sharp reduction in the permeability at a fibre volume fraction of approximately 0.60, in particular for K_1 (along the weft direction). This is supported by the ratio K_1/K_2. For $V_f > 0.60$, it is approximately constant, as implied by a frequently used analytical model for permeability estimation [36], at a mean value of 2.7 with a standard deviation of 0.3. On the other hand, its values are widely scattered between 4.1 and 8.2 for $V_f < 0.60$. This apparent change in properties coincides with an observed change in fabric geometry, suggesting causality between both. For $V_f < 0.60$, the weft yarns on the top and bottom surface (Fig. 10A) are not fully compacted, and V-shaped gaps between the weft yarns, the binder yarns and the tool surfaces facilitate flow. Lack of compaction also allows relatively high variability in gap configuration, resulting in a large scatter in permeability values. At higher V_f, the fabric is completely compacted, and the gaps are closed by deformation of the weft yarns and of the binder yarns (Fig. 10B). This may explain the significant reduction in K_1, which is oriented along the fabric weft yarns and thus is sensitive to reductions in the gap space in this direction.

As the local yarn geometries were defined with high accuracy, the predictions based on the CFD simulations at V_f = 0.55 and V_f = 0.67 show better quantitative agreement with experimental data than those reported by Song et al. [15] in the only comparison between predicted and measured values for 3D textiles found in the literature. Comparison of the experimental data with fitted analytical curves based on a Kozeny-Carman type relation [36] indicates that the apparent strong dependence of K_1 on V_f for this fabric is not described by analytical permeability models which assume unchanging geometrical yarn configuration with increasing V_f. More detailed numerical analysis is required to account for the observed change in binder configuration on the fabric surface and its effect on the permeability.

5. Composite mechanical analysis

5.1 Method

At the unit cell level, textile composites are modelled with two constituents, transversely isotropic composite yarns (i.e. filaments at a given packing density in a matrix of cured resin) and an isotropic elastic matrix in inter-yarn gaps. Modelling is based on the nominal properties of a cured epoxy resin (Gurit Prime 20LV) and of a carbon fibre (Torayca T300) as listed in Table 3. The transverse modulus of the carbon fibre, which is not given by the supplier, was assumed to be 15 GPa. Whilst this value is taken from published experimental data [37] for a similar type of carbon fibre, the sensitivity of the transverse modulus of the composite to variations in the transverse modulus of filaments can be estimated to be relatively small [37].

The data in Table 3 were used as input for mechanical analysis based on an idealised hexagonal single filament model. Under the assumption that the global fibre volume fraction in the unit cell is $V_f = 0.55$, i.e. the composite has a thickness $H = 5.0$ mm, the fibre volume fraction in the yarn was set to the corresponding value $V_f = 0.66$. The elastic constants for a composite yarn were derived from solving the six load cases for principal tensile and shear stresses using the implicit static finite element (FE) code ABAQUS®. While application of micromechanics equations, as compiled e.g. by Murthy and Chamis [38], should give equivalent results, the single filament FE model was used since it will allow additional simulation of viscoelastic effects and defect inclusion in future work.

In addition, the longitudinal strength of the composite yarn is identified as the stress at fracture of the fibre (at a strain of 1.5 %, Table 3). The transverse tensile strength of the composite yarn was assumed to be equal to the tensile strength of cured resin, while the longitudinal shear strength was equal to the interlaminar shear strength (Table 3). The effective yarn properties are summarised in Table 4.

Based on these data, a continuum damage model introduced by Ruijter [39] was implemented to reduce the yarn stiffness gradually by defining the modulus (in any direction) as

$$E = E_0 \max(P, 0.001) \quad , \tag{5}$$

where E_0 is the initial value and P represents a penalty function. The chosen continuum damage mechanics model describes stiffness degradation similar to Puck's phenomenological failure theory [40] instead of utilising an approach based on fracture mechanics. The latter approach would require values of fracture toughness and energy release rate as additional input data, the determination of which requires extensive experimental work, while the model implemented here requires only one phenomenological parameter. The usefulness of this model was proven through application for accurate prediction of the performance of a composite with a plain weave fabric as reinforcement [41]. In axial loading, yarn failure is dominated by the brittle properties of the fibres, such that

$$P = \begin{cases} 1, & D_1 \le 1 \\ 0.001, & D_1 > 1 \end{cases} \quad . \tag{6}$$

The axial damage parameter, D_1, is determined from the maximum stress according to

$$D_1 = \max\left(\frac{\sigma_{11}}{F_{11}^t}, -\frac{\sigma_{11}}{F_{11}^c} \right) \quad . \tag{7}$$

In transverse or shear loading, the yarn stiffness is reduced gradually due to matrix failure. The penalty function is modelled as

$$P = 1 - \frac{1}{\exp(-c_1 D + c_2)} \quad , \tag{8}$$

where c_1 = 8 and c_2 = 13 are empirical constants, and the damage parameter, D, can have values D_2 or D_3 (for shear or transverse loading, respectively). In shear, damage is derived from the partial distortion energy

$$D_2 = \frac{\sqrt{\sigma_{12}^2 + \sigma_{13}^2}}{F_{12}} \quad , \tag{9}$$

while the maximum principal stress criterion

$$D_3 = \max\left(\frac{\max(\sigma_{22}, \sigma_{33})}{F_{22}^t}, -\frac{\min(\sigma_{22}, \sigma_{33})}{F_{22}^c} \right) \tag{10}$$

is applied for transverse loading.

In inter-yarn gaps, failure of the resin matrix was described based on the von Mises criterion. Degradation of the matrix stiffness follows the same law as for the transverse yarn stiffness, which is described in Eq. (8).

5.2 Results and discussion

For FE analysis to predict the mechanical in-plane properties of composites with the orthogonal weave as reinforcement (one fabric layer at H = 5.0 mm, i.e. V_f = 0.55), composite yarn or matrix properties as discussed in Section 5.1 were assigned locally at the appropriate orientations to a voxel mesh of the composite unit cell (Fig. 11). Loading of the unit cell beyond failure (maximum strain 2 %) was simulated by setting appropriate periodic boundary conditions [42] in the warp and weft direction and free boundaries for the top and bottom surfaces.

Preliminary simulations using the same voxel mesh as used for the flow simulations in Section 4 indicated that local misassignment of properties, in particular near points of contact between binder yarns and weft yarns, resulted in artificially reduced failure strain (at approximately 1 %). Thus, the mesh was refined by doubling the number of elements in the fabric warp direction. In addition, manual corrections were made to the mesh to ensure that no local misassignment of properties to the voxels occurred. Assessing several mesh densities indicated that a convergent solution with the results plotted in Fig. 12 and listed in Table 5 was obtained for this model (with maximum allowed time increment in the implicit solution for static stress analysis in ABAQUS® set to 2.5×10^{-3}). For tensile loading in both fabric directions, reasonable agreement between simulated and corresponding experimental values, measured according to European Standard EN ISO 527-4:1997 using specimens made by Resin Transfer Moulding, was found for tensile strength and modulus. While conformal meshing of realistic unit cell geometries is unattainable, it is to be noted that the voxel mesh approach may introduce artificial sharp edges at yarn/matrix interfaces resulting in stress concentrations. A voxel smoothing approach was proposed by Potter et al. [43] as a possible solution. However, for the case of the 3D orthogonal weave studied here, the yarns have largely rectangular tow cross-sections and follow straight paths. In this particular case, the voxel mesh represents the geometry with sufficient accuracy while avoiding artificial stress concentrations. However, for loading in weft direction, the predicted onset of unit cell stiffness reduction at a strain of 0.7 % is not reflected in the experimental data (Fig. 12B). It can be speculated that this difference is related to the boundary conditions in testing (in particular imperfect alignment), which may result in successive rather than simultaneous failure of all unit cells in actual tensile specimens.

To understand mechanisms of damage initiation, failed tensile specimens were investigated using Scanning Electron Microscopy (SEM). It was observed (Fig. 13) that, for in-plane loading in the warp or weft direction, the fracture surfaces were always located in planes containing binder yarns travelling through the reinforcement thickness, indicating that damage was initiated around the binders. Similar fracture initiation and subsequent damage development was predicted by the simulations, despite using a voxel mesh and implementation of a simple failure model. The reasonable quantitative accuracy of predictions for the in-plane tensile strength can be attributed mainly to the realistic models with high level of geometrical detail. As pointed out by Mouritz and Cox [44], local fibre misalignment because of the presence of the binder may give rise to local axial shear stresses and may cause plastic strain as irreversible matrix deformation. Further studies are required to investigate in more detail the relation between composite strength at the unit cell scale and fabric architecture.

Comparison of calculated properties in warp and weft direction indicates that the failure strain, which is dominated by the brittle fibres, is similar in both directions at 1.31 % and 1.26 %, respectively. For the strength in both fabric directions, the ratio F_{weft}/F_{warp} would be expected to be 1.03, reflecting the ratio of fibre volume fractions for 7 layers in weft direction and 6 layers in warp direction, if all yarns were perfectly straight. The actual ratio, F_{weft}/F_{warp} = 0.76, is similar to the ratio of fibre volume fractions, V_{fweft}/V_{fwarp} = 0.74, for 5 layers in weft direction and 6 layers in warp direction. This implies that the two crimped surface layers in weft direction contribute little to the composite strength.

6. Conclusions

For the example of a 3D orthogonal weave reinforcement, representative geometrical parameters were quantified experimentally at different compaction levels by detailed μ-CT image analysis. Unit cell models at high level of geometrical detail, including systematic local variations in yarn paths and yarn cross-sections, were generated in TexGen in a novel semi-automated manner and discretised into voxels. Based on these models, CFD simulation of impregnating flow and static mechanical analysis were carried out for prediction of the in-plane permeability of the fabric and in-plane tensile properties of finished composites, respectively. With inclusion of local variations in geometrical modelling, the predictions of fabric permeability improved significantly compared with the experimental data. The results indicated that the binder configuration on the fabric surfaces, which changes with increasing degree of fabric compression, has a significant effect on the permeability, in particular in weft direction. Composite in-plane strength predictions based on static mechanical analyses showed good quantitative agreement with experimental results. Reduced strength in weft direction compared to the warp direction is caused mainly by crimp in the fabric surface layers, which is related to localised yarn compression at cross-over points with the binder.

Acknowledgements

This work was supported by the Engineering and Physical Sciences Research Council [grant number: EP/IO33513/1], through the EPSRC Centre for Innovative Manufacturing in Composites. The 3D woven fabric was supplied by Airbus UK.

References

1. Mouritz AP, Bannister MK, Falzon PJ, Leong KH. Review of applications for advanced three-dimensional fibre textile composites. *Compos Part A-Appl S* 1999; 30(12): 1445-1461.
2. Lomov SV, Bogdanovich AE, Ivanov DS, Mungalov D, Karahan M, Verpoest I. A comparative study of tensile properties of non-crimp 3D orthogonal weave and multi-layer plain weave E-glass composites. Part 1: Materials, methods and principal results. *Compos Part A-Appl S* 2009; 40(8): 1134–1143.
3. Ivanov DS, Lomov SV, Bogdanovich AE, Karahan M, Verpoest I. A comparative study of tensile properties of non-crimp 3D orthogonal weave and multi-layer plain weave E-glass composites. Part 2: Comprehensive experimental results. *Compos Part A-Appl S* 2009; 40(8): 1144-1157.
4. Tan P, Tong L, Steven GP, Ishikawa T. Behavior of 3D orthogonal woven CFRP composites. Part I. Experimental investigation. *Compos Part A-Appl S* 2000; 31(3): 259-271.
5. Tan P, Tong L, Steven GP. Behavior of 3D orthogonal woven CFRP composites. Part II. FEA and analytical modeling approaches. *Compos Part A-Appl S* 2000; 31(3): 273-281.
6. Carvelli V, Gramellini G, Lomov SV, Bogdanovich AE, Mungalov DD, Verpoest I. Fatigue behaviour of non-crimp 3D orthogonal weave and multi-layer plain weave E-glass reinforced composites. *Compos Sci Technol* 2010; 70(14): 2068-2076.
7. Luo Y, Lv L, Sun B, Qiu Y, Gu B. Transverse impact behavior and energy absorption of three-dimensional orthogonal hybrid woven composites. *Compos Struct* 2007; 81(2): 202-209.
8. Mohamed MH, Wetzel KK. 3D Woven Carbon/Glass Hybrid Spar Cap for Wind Turbine Rotor Blade, *J Sol Energ - T ASME* 2006; 128(4): 562-573.
9. Carvelli V, Pazmino J, Lomov SV, Verpoest I. Deformability of a non-crimp 3D orthogonal weave E-glass composite reinforcement. *Compos Sci Technol* 2012; 73: 9-18.
10. Parnas RS, Flynn KM, Dal-Favero ME. A Permeability Database for Composites Manufacturing. *Polym Composite* 1997; 18(5): 623-633.
11. Potluri P, Sagar TV. Compaction modelling of textile preforms for composite structures. *Compos Struct* 2008; 86(1-3): 177-185.
12. Endruweit A, Long AC. Analysis of Compressibility and Permeability of Selected 3D Woven Reinforcements. *J Compos Mater* 2010; 44(24): 2833-2862.
13. Mohamed M. 3D Woven Carbon-Glass Hybrid Wind Turbine Blades. In: *Wind Turbine Blade Workshop*, Albuquerque, 2004.
14. Ngo ND, Tamma KK. Complex three-dimensional microstructural permeability prediction of porous fibrous media with and without compaction. *Int J Numer Meth Eng* 2004; 60(10): 1741-1757.
15. Song YS, Chung K, Kang TJ, Youn JR. Prediction of permeability tensor for three dimensional circular braided preform by applying a finite volume method to a unit cell. *Compos Sci Technol* 2004; 64(10-11): 1629-1636.
16. Bale H, Blacklock M, Begley MR, Marshall DB, Cox BN, Ritchie RO, Kerans R. Characterizing Three-Dimensional Textile Ceramic Composites Using Synchrotron X-Ray Micro-Computed-Tomography. *J Am Ceram Soc* 2012; 95(1): 392-402.
17. Karahan M, Lomov SV, Bogdanovich AE, Mungalov D, Verpoest I. Internal geometry evaluation of non-crimp 3D orthogonal woven carbon fabric composite. *Compos Part A-Appl S* 2010; 41(9): 1301–1311.
18. Badel P, Vidal-Salle E, Maire E, Boisse P. Simulation and tomography analysis of textile composite reinforcement deformation at the mesoscopic scale. *Compos Sci Technol* 2008; 68(12): 2433-2440.
19. Mahadik Y, Brown KAR, Hallett S.R. Characterisation of 3D woven composite internal architecture and effect of compaction. *Compos Part A-Appl S* 2010; 41(7): 872-880.
20. Blacklock M, Bale H, Begley M, Cox B. Generating virtual textile composite specimens using statistical data from micro-computed tomography: 1D tow representations for the Binary Model. *J Mech Phys Solids* 2012; 60(3): 451-470.
21. Loix F, Badel P, Orgéas L, Geindreau C, Boisse P. Woven fabric permeability: From textile deformation to fluid flow mesoscale simulations. *Compos Sci Technol* 2008; 68(7-8): 1624-1630.
22. Mahadik Y, Hallett SR. Finite element modelling of tow geometry in 3D woven fabrics. *Compos Part A-Appl S* 2010; 41(9): 1192-1200.
23. Tsukrov I, Bayraktar H, Giovinazzo M, Goering J, Gross T, Fruscello M, Martinsson L. Finite Element Modeling to Predict Cure-Induced Microcracking in Three-Dimensional Woven Composites. *Int J Fracture* 2011; 172(2): 209-216.
24. Desplentere F, Lomov S, Woerdeman D, Verpoest I, Wevers M, Bogdanovich A. Micro-CT characterization of variability in 3D textile architecture. *Compos Sci Technol* 2005; 65(13): 1920-1930.
25. Long AC, Brown LP. Modelling the geometry of textile reinforcements for composites: TexGen. In: Boisse, editor. *Composite reinforcements for optimum performance*. Cambridge: Woodhead Publishing, 2011. p. 239-264.
26. TexGen (Version 3.5.2). University of Nottingham; 2012. <http://texgen.sourceforge.net> [viewed 27.09.2012].

27. Weisstein EW. Superellipse. From *MathWorld--A Wolfram Web Resource.* Wolfram Research, Inc.; 1999-2012. <http://mathworld.wolfram.com/Superellipse.html> [viewed 02.10.2012].
28. Verleye B, Croce R, Griebel M, Klitz M, Lomov S, Morren G, Sol H, Verpoest I, Roose D. Permeability of textile reinforcements: Simulation, influence of shear and validation. *Compos Sci Technol* 2008; 68(13): 2804-2810.
29. Glatt E, Rief S, Wiegmann A, Knefel M, Wegenke E. Structure and pressure drop of real and virtual metal wire meshes. Bericht des Fraunhofer ITWM 157, 2009.
30. Jaganathan S, Vahedi Tafreshi H, Pourdeyhimi B. A realistic approach for modeling permeability of fibrous media: 3-D imaging coupled with CFD simulation. *Chem Eng Sci* 2008; 63(1): 244-252.
31. Kim HJ, Swan CC. Voxel-based meshing and unit-cell analysis of textile composites. *Int J Numer Meth Eng* 2003; 56(7): 977-1006.
32. Ernst G, Vogler M, Hühne C, Rolfes R. Multiscale progressive failure analysis of textile composites. *Compos Sci Technol* 2010; 70(1): 61-72.
33. Gebart BR. Permeability of Unidirectional Reinforcements for RTM. *J Compos Mater* 1992; 26(8): 1100-1133.
34. Grouve WJB, Akkerman R. An idealised bc for the meso scale analysis of textile impregnation processes. In: *The 9th International Conference on Flow Processes in Composite Materials*. Montréal; 2008.
35. Beavers GS, Joseph DD. Boundary conditions at a naturally permeable wall. *J Fluid Mech* 1967; 30(1): 197-207.
36. Carman PC. Fluid Flow through Granular Beds. *T I Chem Eng-Lond* 1937; 15: 150-156.
37. Maurin R, Davies P, Baral N, Baley C. Transverse Properties of Carbon Fibres by Nano-Indentation and Micro-mechanics. *Appl Compos Mater* 2008; 15(2): 61-73.
38. Murthy PLN, Chamis CC. Integrated Composite Analyser (ICAN). Users and Programmers Manual. NASA Technical Paper 2514, 1986.
39. Ruijter W. Analysis of mechanical properties of woven textile composite as functions of textile geometry. PhD dissertation, School of M3, University of Nottingham, Nottingham, 2008.
40. Puck A, Schürmann H. Failure analysis of frp laminates by means of physically based phenomenological models. *Compos Sci Technol* 1998; 58(7): 1045-1067.
41. Matveev MY, Long AC, Jones IA. Mechanical properties of textile composites with variability in micromechanical properties. In: 15th European Conference on Composite Materials. Venice, 2012
42. Li S, Zhou C, Yu H, Li L. Formulation of a unit cell of a reduced size for plain weave textile composites. *Comp Mater Sci* 2011; 50(5): 1770-1780.
43. Potter E, Pinho ST, Robinson P, Iannucci L, McMillan AJ. Mesh generation and geometrical modelling of 3D woven composites with variable tow cross-sections. *Comp Mater Sci* 2012; 51(1): 103-111.
44. Mouritz AP, Cox BN. A mechanistic interpretation of the comparative in-plane mechanical properties of 3D woven, stitched and pinned composites. *Compos Part A-Appl S* 2010; 41(6): 709-728.

Table 1. Specifications of 3D reinforcement characterised here.

Fabric style	Orthogonal weave
Areal density / kg/m^2	4.775
Number of warp layers	6
Warp yarn	12K
Warp yarn linear density / g/km	800
Number of weft layers	7
Weft yarn	6K × 2
Weft yarn linear density / g/km	800
Binder yarn	1K
Binder yarn linear density / g/km	67

Table 2. Geometry parameters measured for the orthogonal reinforcement at different compression levels; average value, standard deviation and coefficient of variation (standard deviation / average) are given where appropriate.

	Number of measurements	Yarn width / mm	Yarn height / mm	n in power ellipse (Eq. 3)	Yarn gap / mm
$H = 5.0$ mm, $V_f = 0.55$					
Warp	10755	1.88 ± 0.04 (± 2 %)	0.41 ± 0.05 (± 11 %)	0	0.33 ± 0.05 (± 14 %)
Surface layer weft	39	2.13 ± 0.06 (± 3 %)	0.39 ± 0.03 (± 8 %)	1.4 / 0	0.32 ± 0.07 (± 22 %)
Internal layer weft	4299	2.09 ± 0.08 (± 4 %)	0.35 ± 0.06 (± 16 %)	0.1	0.28 ± 0.06 (± 16 %)
Surface section binder	4	0.62 ± 0.05 (± 9 %)	0.15 ± 0.02 (± 10 %)	1	
Internal section binder	119	0.34 ± 0.05 (± 15 %)	0.21 ± 0.03 (± 13 %)	0	
$H = 4.1$ mm, $V_f = 0.67$					
Warp	7319	1.90 ± 0.02 (± 1%)	0.33 ± 0.02 (± 7%)	0	0.14 ± 0.02 (± 17 %)
Surface layer weft	23	2.32 ± 0.10 (± 4 %)	0.29 ± 0.20 (± 8 %)	1.2 / 0.5	0.08 ± 0.02 (± 25 %)
Inner layer weft	5264	2.24 ± 0.06 (± 3 %)	0.27 ± 0.02 (± 6 %)	0	0.16 ± 0.04 (± 25 %)
Surface section binder	6	0.89 ± 0.06 (± 7 %)	0.07 ± 0.01 (± 10 %)	0	
Internal section binder	116	0.25 ± 0.02 (± 8 %)	0.23 ± 0.03 (± 12 %)	0	

Table 3. Nominal properties of resin matrix and fibres.

	E / GPa	Tensile strength / MPa	Tensile failure strain / %	Interlaminar shear strength / MPa
Cured resin	3.5	73	3.5	47
Fibre: Torayca T300	230	3450	1.5	-

Table 4. Composite yarn properties derived from FE analysis, $V_f = 0.66$.

E_{11} / GPa	E_{22}, E_{33} / GPa	G_{12}, G_{13} / GPa	G_{23} / GPa	v_{12}, v_{13}	v_{23}	F_{11} / MPa	F_{22} / MPa	F_{12} / MPa
152.60	8.15	3.02	2.90	0.300	0.345	2289	73	47

Table 5. Comparison of experimentally determined and calculated strength, F, and modulus, E, of composite under tensile loading in warp and weft direction; average values and standard deviations are given where appropriate.

	warp		weft	
	F / MPa	E / GPa	F / MPa	E / GPa
simulation	833	66	632	59
experiment	791 ± 38	60 ± 2	710 ± 21	58 ± 3

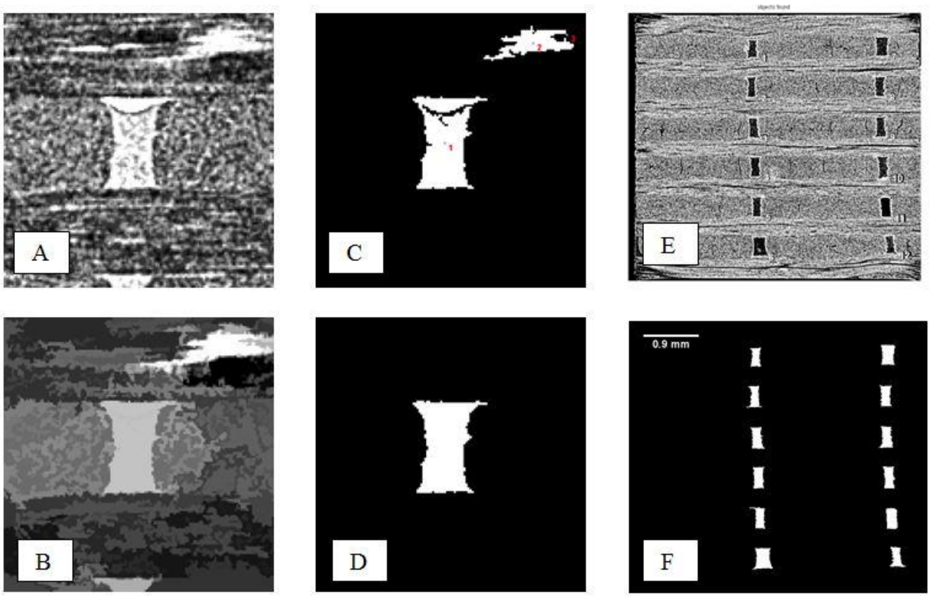

Figure 1. Identification of yarns and inter-yarn gaps in 3D carbon fibre reinforcement; A-D: progressive image operations to isolate gap regions; E: labelled gaps in original μ-CT image; F: binary image of gaps.

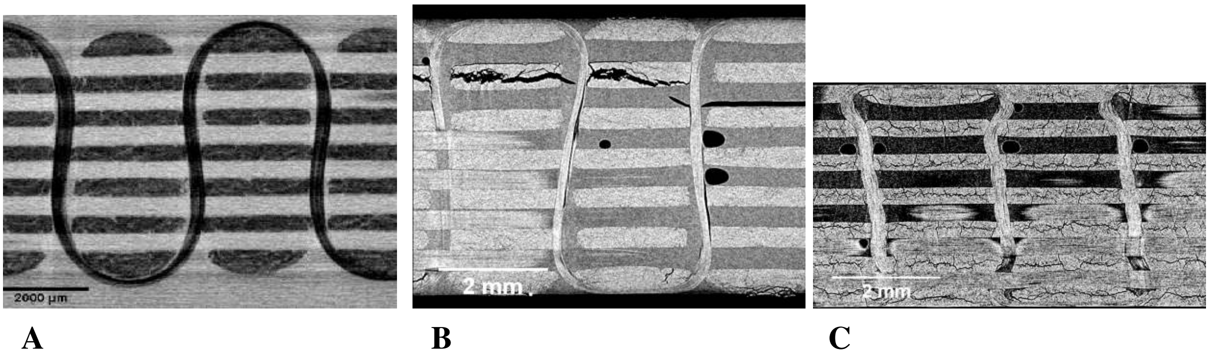

Figure 2. Change in yarn geometry under fabric compaction; A: dry fabric at no compression, thickness H = 6.0 mm; B: composite panel at H = 5.0 mm, V_f = 0.55; C: composite panel at H = 4.1 mm, V_f = 0.67.

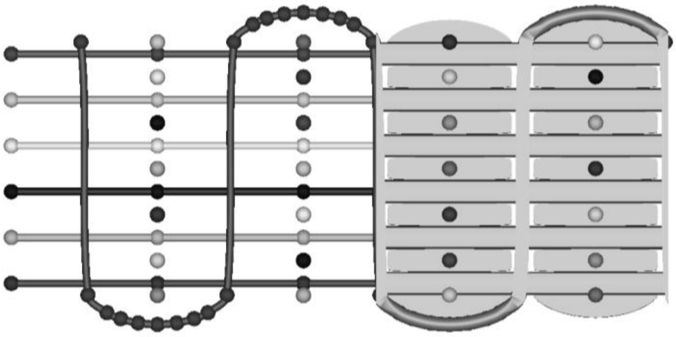

Figure 3. Definition of binder yarn path for 3D orthogonal weave in TexGen.

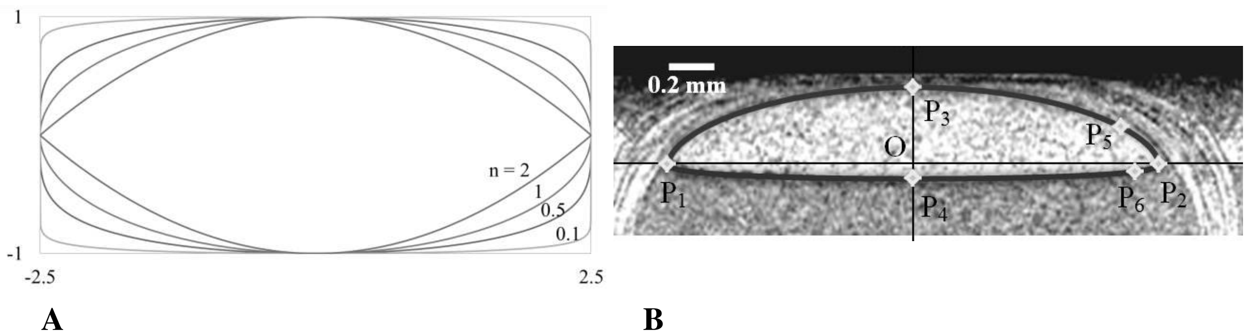

Figure 4. Power-ellipse representing yarn cross-section in 3D orthogonal carbon reinforcement; A: characteristics of power ellipse function at different values of *n*; B: example for hybrid cross-section.

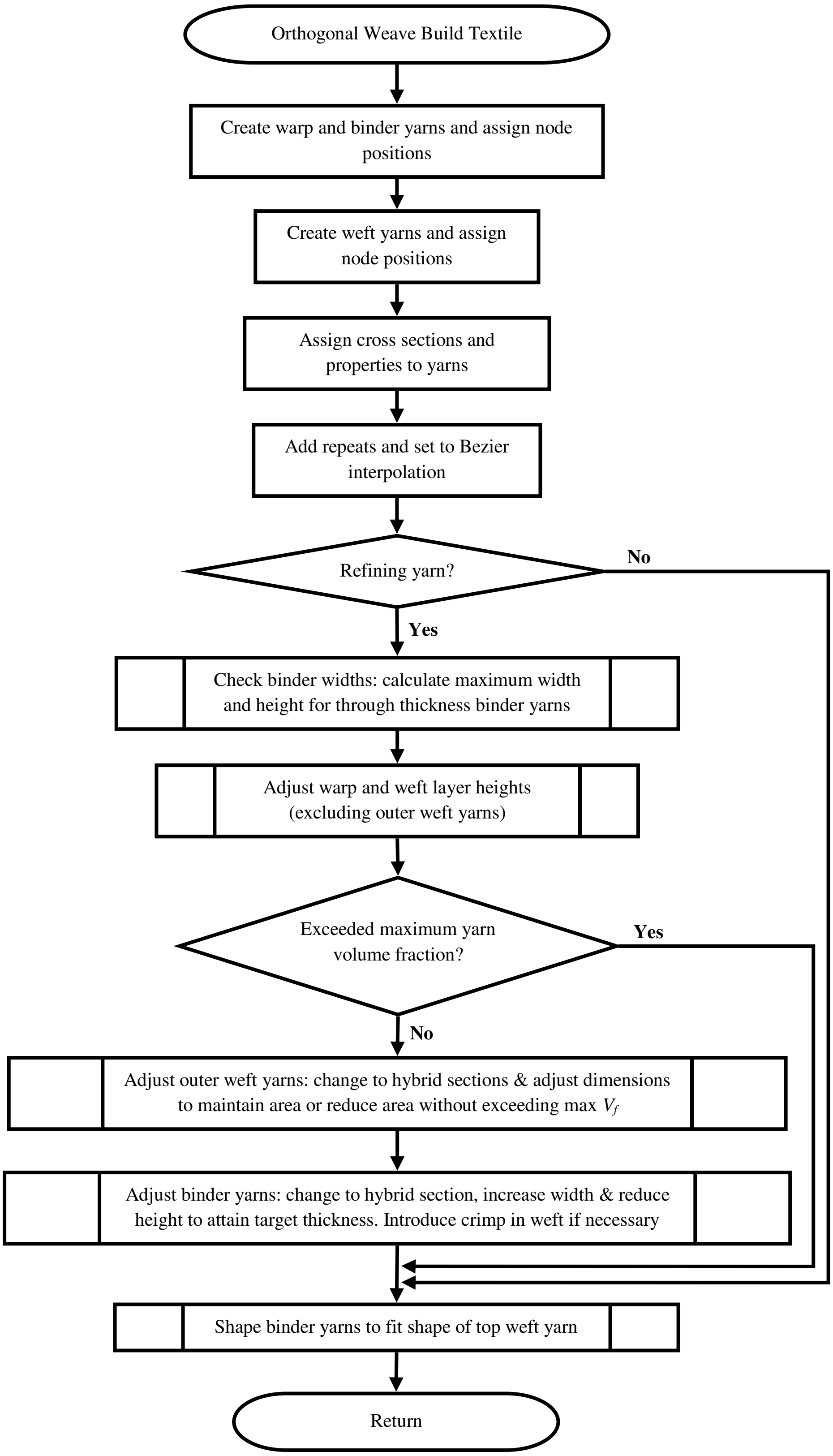

Figure 5. Flowchart for generation of 3D orthogonal weave model with refinement.

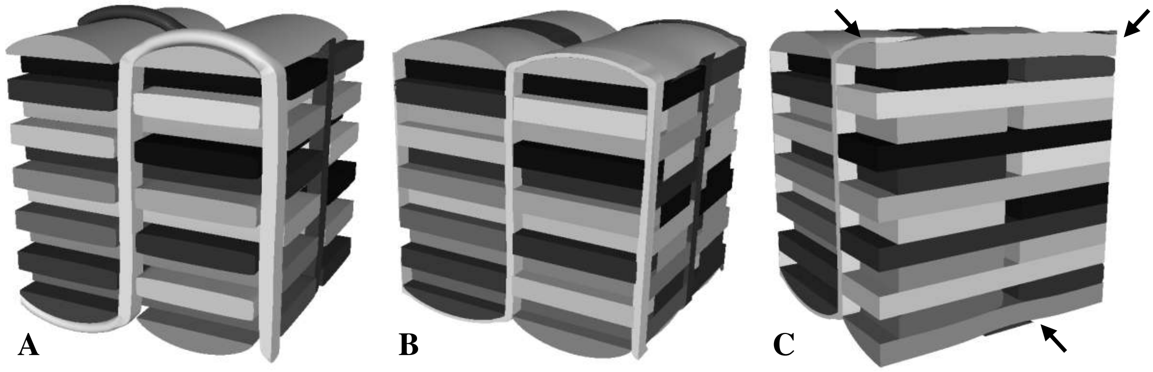

Figure 6. Orthogonal weave generated automatically using TexGen 3DWizard refine option; A: original fabric thickness, H = 6.32 mm; B: H = 5.03 mm; C: H = 4.43 mm; arrows indicate crimp in outer weft yarns.

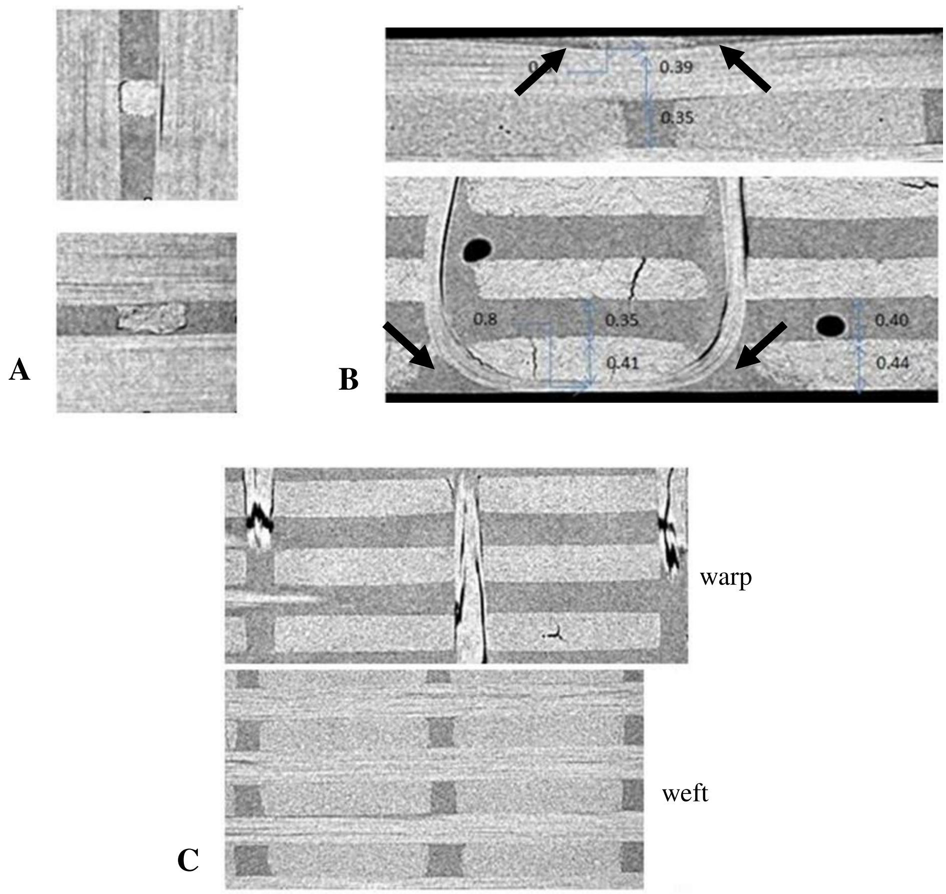

Figure 7. Local geometry variations observed in 3D μ-CT images; A: different binder cross-sections; B: formation of dimples on surface; C: rectangular cross-sections of warp yarns, more rounded cross-sections of weft yarns.

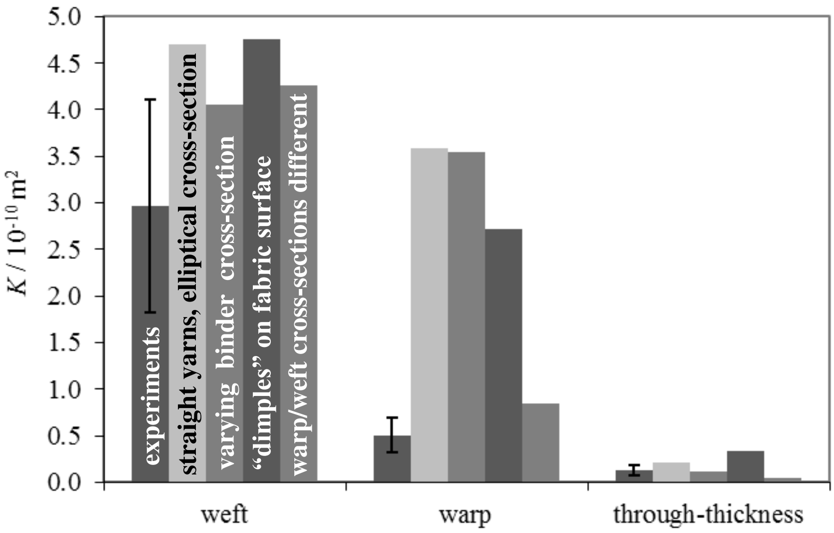

Figure 8. Permeability predictions with incremental local geometry variations, H = 5.0 mm, V_f = 0.55, compared to experimental data; error bars on experimental data indicate standard deviation.

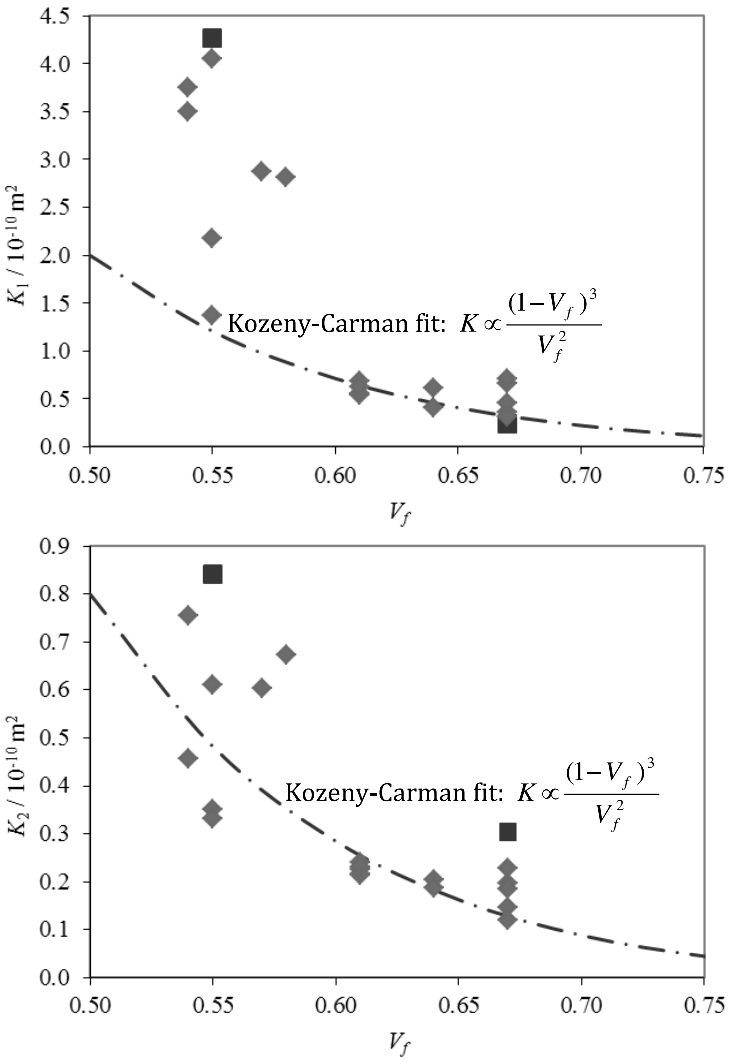

Figure 9. Principal permeability values, K_1 and K_2, as a function of the fibre volume fraction, V_f; square symbols: CFD results; diamond symbols: experimental data; analytical trend lines [34] are also indicated .

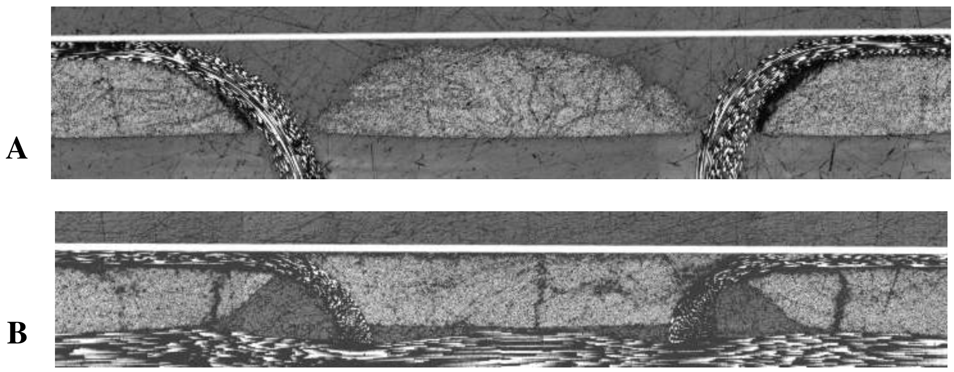

Figure 10. Details of binder and weft yarn configurations on fabric surface at different compaction levels; white lines indicate tool surface; A: H = 5.0 mm, V_f = 0.55; B: H = 4.2 mm, V_f = 0.65.

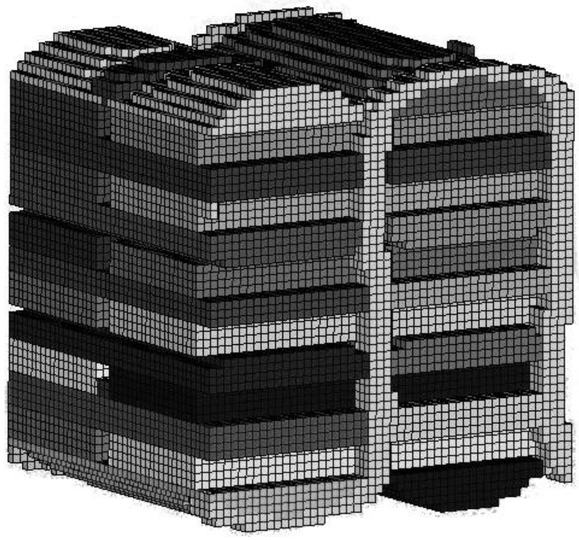

Figure 11. Voxel mesh of fabric unit cell for mechanical analysis; voxels representing resin only are not shown.

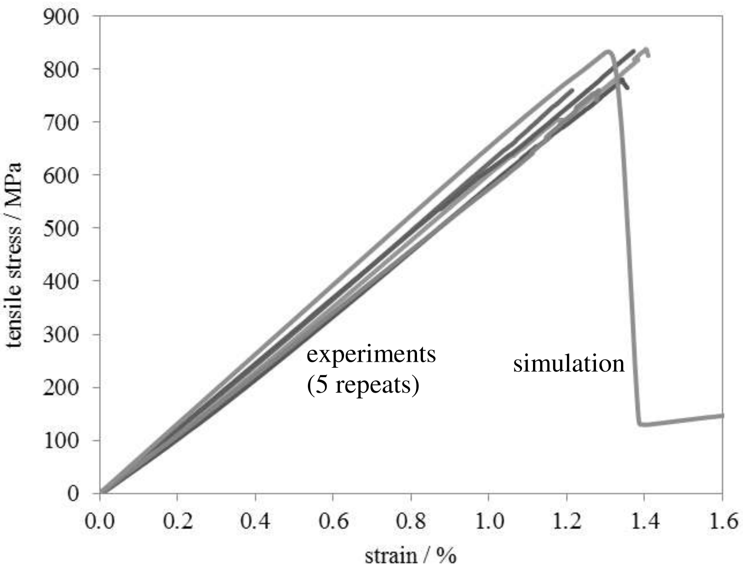

A

B

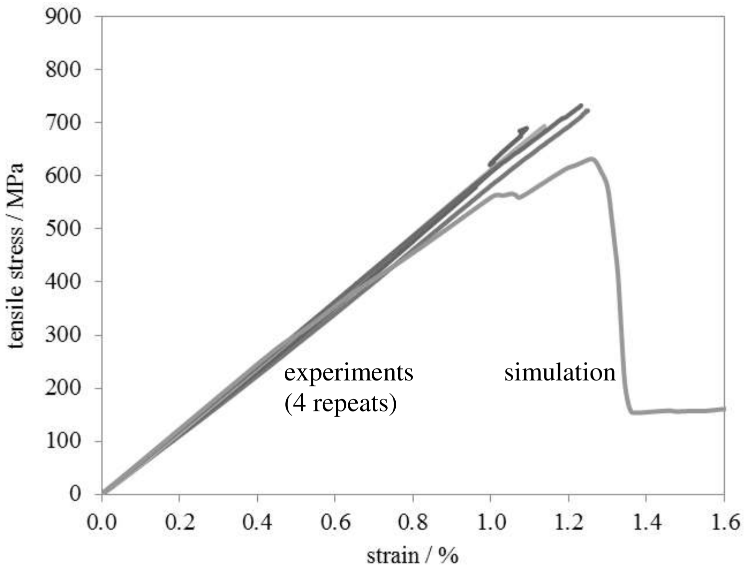

Figure 12. Comparison of experimental and simulated stress-strain curves; A: tensile load in warp direction; B: tensile load in weft direction.

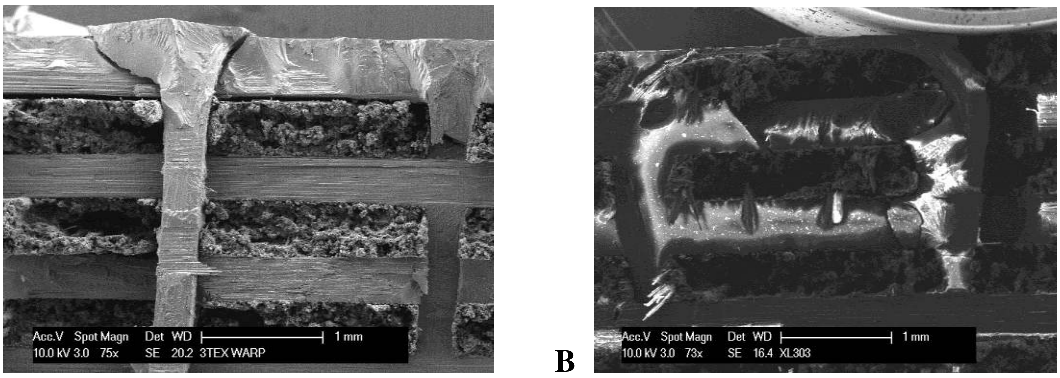

A B

Figure 13. SEM images of fracture surfaces; A: tensile load in warp direction; B: tensile load in weft direction.